



A *NICER* Thermonuclear Burst from the Millisecond X-Ray Pulsar SAX J1808.4–3658

Peter Bult¹, Gaurava K. Jaisawal², Tolga Güver^{3,4}, Tod E. Strohmayer⁵, Diego Altamirano⁶, Zaven Arzoumanian¹, David R. Ballantyne⁷, Deepto Chakrabarty⁸, Jérôme Chenevez², Keith C. Gendreau¹, Sebastien Guillot^{9,10}, and Renee M. Ludlam^{11,12}

¹ Astrophysics Science Division, NASA’s Goddard Space Flight Center, Greenbelt, MD 20771, USA

² National Space Institute, Technical University of Denmark, Elektrovej 327-328, DK-2800 Lyngby, Denmark

³ Department of Astronomy and Space Sciences, Science Faculty, Istanbul University, Beyazit, 34119 Istanbul, Turkey

⁴ Istanbul University Observatory Research and Application Center, Beyazit, 34119 Istanbul, Turkey

⁵ Astrophysics Science Division and Joint Space-Science Institute, NASA’s Goddard Space Flight Center, Greenbelt, MD 20771, USA

⁶ Physics & Astronomy, University of Southampton, Southampton, Hampshire SO17 1BJ, UK

⁷ Center for Relativistic Astrophysics, School of Physics, Georgia Institute of Technology, 837 State Street, Atlanta, GA 30332-0430, USA

⁸ MIT Kavli Institute for Astrophysics and Space Research, Massachusetts Institute of Technology, Cambridge, MA 02139, USA

⁹ CNRS, IRAP, 9 avenue du Colonel Roche, BP 44346, F-31028 Toulouse Cedex 4, France

¹⁰ Université de Toulouse, CNES, UPS-OMP, F-31028 Toulouse, France

¹¹ Cahill Center for Astronomy and Astrophysics, California Institute of Technology, Pasadena, CA 91125, USA

Received 2019 September 8; revised 2019 September 29; accepted 2019 October 4; published 2019 October 23

Abstract

The *Neutron Star Interior Composition Explorer* (*NICER*) has extensively monitored the 2019 August outburst of the 401 Hz millisecond X-ray pulsar SAX J1808.4–3658. In this Letter, we report on the detection of a bright helium-fueled Type I X-ray burst. With a bolometric peak flux of $(2.3 \pm 0.1) \times 10^{-7} \text{ erg s}^{-1} \text{ cm}^{-2}$, this was the brightest X-ray burst among all bursting sources observed with *NICER* to date. The burst shows a remarkable two-stage evolution in flux, emission lines at 1.0 and 6.7 keV, and burst oscillations at the known pulsar spin frequency, with $\approx 4\%$ fractional sinusoidal amplitude. We interpret the burst flux evolution as the detection of the local Eddington limits associated with the hydrogen and helium layers of the neutron star envelope. The emission lines are likely associated with Fe, due to reprocessing of the burst emission in the accretion disk.

Unified Astronomy Thesaurus concepts: X-ray bursts (1814); Millisecond pulsars (1062)

1. Introduction

The prototypical accreting millisecond X-ray pulsar SAX J1808.4–3658 (hereafter SAX J1808), was first discovered through the detection of a thermonuclear (Type I) X-ray burst with the *BeppoSAX* satellite in 1996 September (in’t Zand et al. 1998). With X-ray outbursts recurring every 2–4 yr, this source has been extensively monitored ever since, leading to the first detection of accretion-powered millisecond pulsations (Wijnands & van der Klis 1998), and the confirmation that X-ray burst oscillations correspond with the stellar spin frequency (Chakrabarty et al. 2003).

In each of the eight outbursts from SAX J1808 that occurred between 1996 and 2015, at least one X-ray burst has been detected (in’t Zand et al. 2001; Bult & van der Klis 2015; Patruno et al. 2017; Sanna et al. 2017). The majority of these bursts showed burst oscillations (Bilous & Watts 2018) and were observed near peak luminosity of their respective outbursts, when the accretion rate was $\approx (3\text{--}5) \times 10^{-10} M_{\odot} \text{ yr}^{-1}$ (Bult & van der Klis 2015). Detailed modeling of a well sampled burst train observed with the *Rossi X-ray Timing Explorer* (*RXTE*) in 2002 October (Galloway & Cumming 2006) demonstrated that these events are examples of X-ray bursts in the “delayed helium” regime (Narayan & Heyl 2003; Galloway et al. 2017). In brief, these bursts are due to a thermonuclear flash in a nearly pure helium layer of the neutron star envelope. This layer of helium builds up on a timescale of one to a few days, through a stable β -limited CNO cycle at the base of a hydrogen layer. The hydrogen layer, in turn, is replenished by the continuous accretion of gas supplied by a hydrogen-rich brown dwarf

companion star, which resides in a 2.01 hr orbit around the pulsar (Chakrabarty & Morgan 1998; Bildsten & Chakrabarty 2001).

The X-ray bursts of SAX J1808 have also reliably shown photospheric radius expansion (PRE; see, e.g., Galloway et al. 2008, for a review). Such PRE may drive the ejection of burning ashes, whose presence could cause discrete spectral features in the burst emission (Weinberg et al. 2006; Yu & Weinberg 2018). Measuring such spectral lines gives a window into the thermonuclear burning reactions, and can potentially be used to constrain the neutron star compactness. Additionally, a large fraction of the burst emission is expected to be intercepted and reprocessed by the accretion disk (Ballantyne & Everett 2005; Degenaar et al. 2018; Fragile et al. 2018), providing an opportunity to characterize the state of the accretion disk through the spectrum of the reflected burst emission.

Launched in 2017 June, the *Neutron Star Interior Composition Explorer* (*NICER*; Gendreau & Arzoumanian 2017) combines good spectral resolution with superb time resolution and high throughput in the 0.2–12 keV energy band. These properties make *NICER* an ideal instrument to study the evolution of PRE in Type I X-ray bursts (see, e.g., Keek et al. 2018a, 2018b; Jaisawal et al. 2019), and search for discrete spectral features (Strohmayer et al. 2019). Hence, when SAX J1808 began a new outburst in 2019 August (Bult et al. 2019; Goodwin et al. 2019b; Parikh & Wijnands 2019; Russell et al. 2019), we triggered an extensive *NICER* monitoring campaign. During this campaign we detected two X-ray bursts; the first occurred on August 9 and was relatively faint, the second was seen on August 21 and was much brighter. In this

¹² Einstein Fellow.

Letter we report on the unusual properties of the August 21 X-ray burst. The detailed analysis of the earlier burst and the full *NICER* campaign will be presented elsewhere.

2. Observations

On 2019 August 21 at 02:04 UTC, *NICER* observed a bright X-ray burst from SAX J1808. These data are available under the *NICER* ObsID 2584010501. We processed the data using *NICERDAS* v6a, which is packaged with *HEASOFT* v6.26. We applied standard screening criteria, keeping only those time intervals when the pointing offset was $<54''$, the Earth limb elevation angle was $>15^\circ$, the elevation angle with respect to the bright Earth limb was $>30^\circ$, and the instrument was outside of the geographic region of the South Atlantic Anomaly. Additionally, standard background screening criteria were applied, which reject all epochs where the rate of saturating particle events (overshoots) is greater than $1 \text{ ct s}^{-1} \text{ detector}^{-1}$, or greater than $1.52 \times \text{COR_SAX}^{-0.633}$, where *COR_SAX*¹³ gives the cutoff rigidity of the Earth's magnetic field, in units of GeV c^{-1} . We then applied the *BARYCORR* tool to correct the observed event times to the solar system barycenter, where we used the JPL DE405 planetary ephemeris (Standish 1998) and the optical coordinates of Hartman et al. (2008). Finally, we estimated the background contributions to our data from *NICER* observations of the *RXTE* blank-field regions (Jahoda et al. 2006).

3. Analysis and Results

The X-ray burst onset, t_0 , occurred on MJD 58716.089362 TDB, which was 442 s into a 1063 s continuous exposure. In the following we focus our analysis on this exposure and express all times with respect to the noted onset time.

3.1. Light Curve and Phenomenology

At t_0 the 0.3–10 keV count rate increased rapidly from an averaged 125 ct s^{-1} to $\approx 34,000 \text{ ct s}^{-1}$ over a timespan of ≈ 4.3 s. The peak rate was maintained for ≈ 3.6 s, before the burst began to decay. The subsequent decay progressed on a minute-long timescale: at $t \approx 64$ s the burst rate had dropped to below 5% of the peak rate, and by the end of the available exposure, at $t = 621$ s, the source flux had fallen to 172 ct s^{-1} . While this rate was slightly higher than the averaged preburst rate, the preburst light curve showed a modest upward trend. If we fit this trend with a linear function, then we find that the burst rate decayed to the extrapolated intensity at $t \approx 580$ s.

Two unusual features stand out in the burst light curve (Figure 1). First, it shows a pronounced double-peaked structure, with a local minimum of $\approx 14,000 \text{ ct s}^{-1}$ at $t \approx 13.1$ s and a secondary peak of $\approx 16,500 \text{ ct s}^{-1}$ at $t \approx 15.5$ s. While double-peaked X-ray bursts have commonly been observed, these structures are usually caused by PRE: the temperature of the photosphere temporarily shifts out of the instrument passband, causing an apparent dip in the observed X-ray rate (Grindlay et al. 1980). Given its low-energy coverage, *NICER* is able to follow the temperature of the photosphere throughout the PRE phase, so any observed dip in the light curve is likely due to a dip in bolometric flux

¹³ The *COR_SAX* parameter is based on a model for the cutoff rigidity that was originally developed for the *BeppoSAX* satellite, and has no specific relation to SAX J1808.

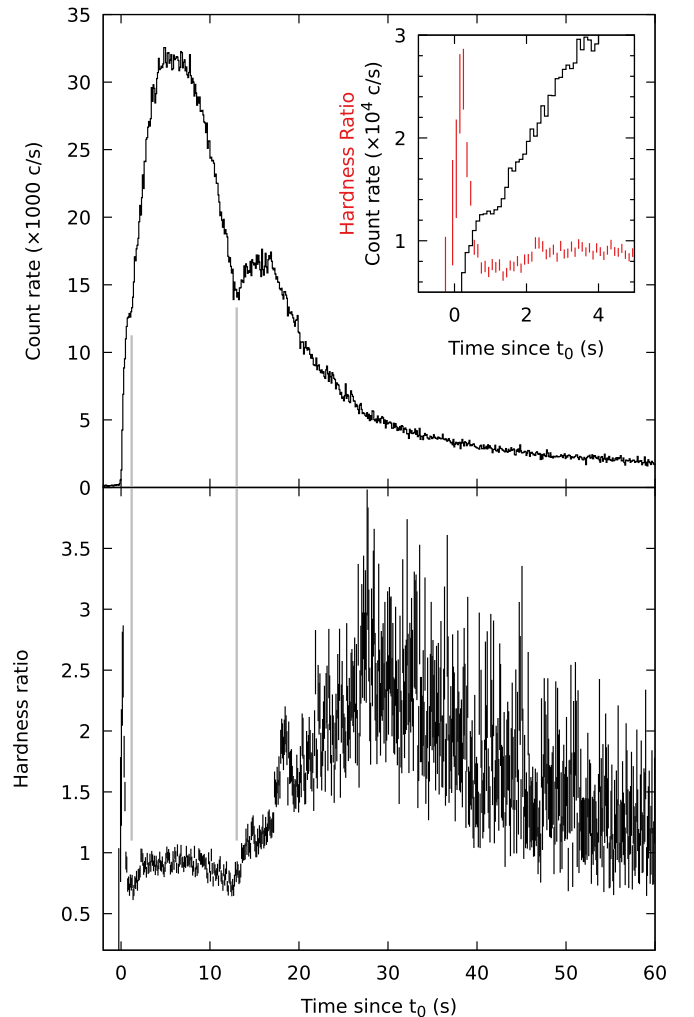


Figure 1. Top: light curve of the X-ray burst from SAX J1808 at 0.1 s time resolution in the 0.3–10 keV energy band. Bottom: hardness ratio, defined as the 3–10 keV rate divided by the 0.3–1 keV rate. Inset: first four seconds of the same data, with the light curve in black (connected line, units of $\times 10^4 \text{ ct s}^{-1}$) and the hardness ratio in red (vertical dashes). All panels are relative to $t_0 = 58716.089362$ TDB. Vertical gray lines were added to guide the eye.

(Keek et al. 2018b; Jaisawal et al. 2019). We investigate this in Section 3.4.

Second, there is a noticeable pause during the rise to the first peak. Initially, the flux increases rapidly; however, between $t \approx 0.6$ s and $t \approx 1.3$ s, this rise briefly stalls, with the count rate remaining constant at $\approx 13,600 \text{ ct s}^{-1}$. After this pause, the rate continues to increase toward the maximum, albeit at a slightly slower pace (Figure 1, inset of top panel). Simultaneously, the hardness ratio (the 3–10 keV rate over the 0.3–1 keV rate) evolves dramatically. As the count rate begins to rise, the hardness ratio spikes. Subsequently, the hardness ratio briefly dips, and then stabilizes. It is during the dip that the pause in count rate is observed. Additionally, the previously mentioned dip in count rate (at $t \approx 13$ s), coincides with a similar dip in the hardness ratio, suggesting these two features are related.

3.2. Preburst Emission

We extracted a spectrum from 400 s prior to the burst and modeled it in *XSPEC* v12.10 (Arnaud 1996). Following

Di Salvo et al. (2019), we find that the spectrum could be well described with the model

$$\text{tbabs}(\text{diskbb} + \text{nthcomp}),$$

where the `tbabs` interstellar absorption model (Wilms et al. 2000) was used with the photoelectric cross-sections of Verner et al. (1996), `diskbb` (Makishima et al. 1986) is a multicolor disk blackbody component, and `nthcomp` (Zdziarski et al. 1996; Życki et al. 1999) is a thermal Comptonization component. We used an absorption column density of $N_{\text{H}} = 2.1 \times 10^{21} \text{ cm}^{-2}$ (Papitto et al. 2009; Di Salvo et al. 2019), and electron temperature of 30 keV (Di Salvo et al. 2019). We further tied the `nthcomp` photon seed temperature to the disk temperature. Our best-fit had a reduced χ^2 (χ_r^2) of 1.04 for 375 degrees of freedom (dof), yielding an inner disk temperature of $kT = 0.70 \pm 0.07 \text{ keV}$ and a power-law photon index of $\Gamma = 2.0 \pm 0.4$. Using the `cflux` model we further measured the unabsorbed 1–10 keV flux to be $(2.85 \pm 0.05) \times 10^{-10} \text{ erg s}^{-1} \text{ cm}^{-2}$, from which we extrapolate a bolometric flux (0.01–100 keV) of $(4.7 \pm 0.5) \times 10^{-10} \text{ erg s}^{-1} \text{ cm}^{-2}$. Assuming a distance of 3.5 kpc (Galloway & Cumming 2006), a $1.4 M_{\odot}$ neutron star mass, and a 10 km radius, this corresponds to a mass accretion rate of $\dot{M} = 2.9 \times 10^{-11} M_{\odot} \text{ yr}^{-1}$, which is $\approx 0.3\%$ of the (hydrogen) Eddington rate.

3.3. Burst Spectroscopy

We investigated the spectral shape of the burst emission by extracting a spectrum from a 4 s interval at the peak of the burst (Figure 2). We first attempted to model this spectrum by adding a blackbody component to the preburst spectrum model, holding all parameters except for those of the blackbody constant. At a χ_r^2 of 28 for 631 dof, this model failed to account for a large excess below 1.5 keV and above 5 keV.

In an attempt to account for the residuals we applied a free scaling factor to the components describing the preburst spectrum (Worpel et al. 2013), so that our model was

$$\text{tbabs}(\text{bbodyrad} + f(\text{diskbb} + \text{nthcomp})),$$

where `bbodyrad` is a blackbody component with its normalization proportional to surface area. At a χ_r^2 of 5.4 for 630 dof, this model failed to remove the large residuals. Additionally, at $f = 159$, the magnitude of the obtained scaling factor is not realistic, as it is much larger than the $f \sim 2\text{--}10$ that is typically observed (Worpel et al. 2013).

In an alternative approach to account for the large soft excess, we adopted a model consisting of the fixed preburst model plus two blackbody components. This model provided a much better description of the data (χ_r^2 of 1.11 for 628), yielding a blackbody with a temperature and radius of $0.233 \pm 0.003 \text{ keV}$ and $318 \pm 5 \text{ km}$, respectively, for the soft excess, and $1.83 \pm 0.03 \text{ keV}$ and $14.7 \pm 0.3 \text{ km}$, respectively, for the higher energy emission (presumably the photosphere). Some structure still remained in the residuals, most prominently at 1.0 and 6.5 keV. The fit was significantly improved (χ_r^2 of 1.07 for 624 dof) by adding a `diskline` component (Fabian et al. 1989) at $6.7_{-0.3}^{+0.1} \text{ keV}$, along with a Gaussian line at $1.05 \pm 0.02 \text{ keV}$. The signal strength of the `diskline` was insufficient to reliably constrain the disk radius and inclination, giving respective limits of $<13 r_g$ and $>65^\circ$. Instead, we fixed

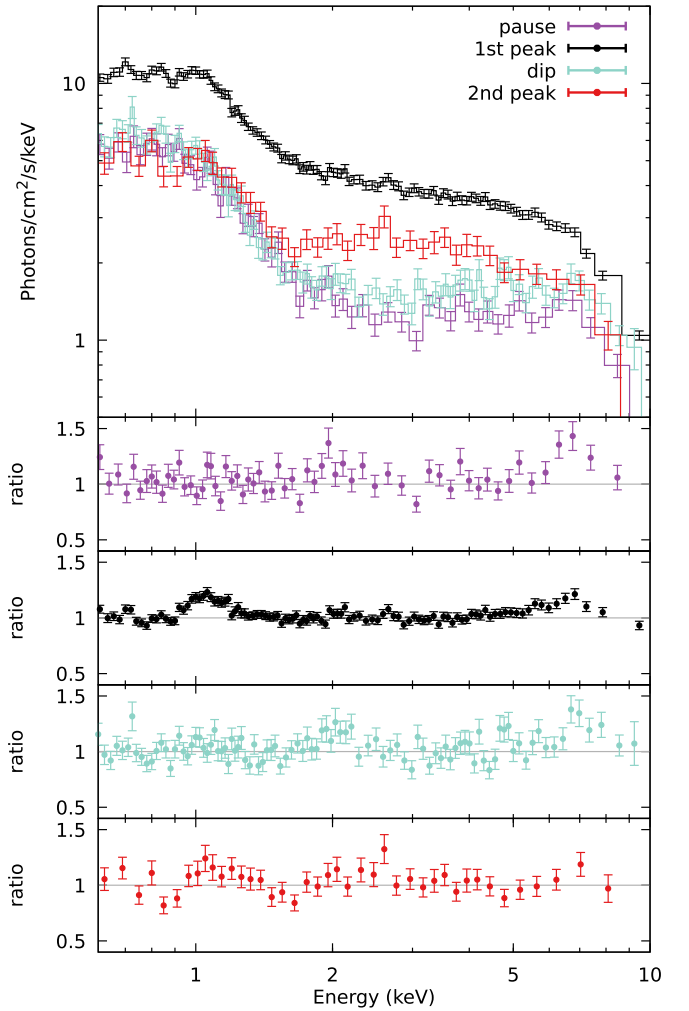


Figure 2. Top: burst spectra at four epochs during the X-ray burst. Bottom: the residuals of the best-fit models, showing the ratio of the data over the model prediction. In each case we have set the normalization of the emission line components to zero, which highlights these lines in the residuals.

the inner radius to $11 r_g$, which is the approximate magnetospheric radius (Bult & van der Klis 2015), and the inclination to 65° , which is within the range allowed by modeling of the Fe K line in the persistent emission of SAX J1808 (Cackett et al. 2009; Papitto et al. 2009; Di Salvo et al. 2019). We further note that while this inclination is inconsistent with the $\leq 30^\circ$ limit derived by Galloway & Cumming (2006), a more sophisticated analysis of the same burst data yielded 69_{-2}^{+4} (Goodwin et al. 2019a). With these parameters held constant, we obtained a line normalization of $0.62 \pm 0.16 \text{ ph cm}^{-2} \text{ s}^{-1}$. Meanwhile, the 1 keV Gaussian line had a normalization of $0.27 \pm 0.07 \text{ ph cm}^{-2} \text{ s}^{-1}$ and standard deviation of $0.05_{-0.02}^{+0.07} \text{ keV}$.

In an attempt to apply a physical foundation to our modeling of these data, we also fit the spectrum using the reflection models of Ballantyne (2004). This overall model is summarized as

$$\text{tbabs}(\text{bbodyrad} + \text{diskbb} + \text{nthcomp} + \text{rdblur} * \text{atable}\{\text{reflection}\})$$

where `rdblur` is a convolution component that applies the relativistic effects associated with an accretion disk around a compact object, and the reflection component tabulates

Table 1
Spectroscopy of the X-Ray Burst

Component	Parameter	Unit	Main Peak	Pause	Dip	Second Peak
Soft blackbody	temperature	keV	0.233 ± 0.003	0.228 ± 0.007	0.210 ± 0.005	0.22 ± 0.01
Soft blackbody	normalization	km	318 ± 5	240 ± 17	297 ± 18	236 ± 31
Hard blackbody	temperature	keV	1.83 ± 0.03	2.5 ± 0.2	2.52 ± 0.14	1.99 ± 0.11
Hard blackbody	normalization	km	14.7 ± 0.3	6.2 ± 0.5	6.8 ± 0.4	10.5 ± 0.7
Gaussian line	line energy	keV	1.05 ± 0.02			1.05 ± 0.02
Gaussian line	standard deviation	keV	$0.05^{+0.07}_{-0.02}$			0.07 ± 0.02
Gaussian line	normalization	ph cm ⁻² s ⁻¹	0.27 ± 0.07			0.26 ± 0.07
Diskline	line energy	keV	$6.7^{+0.1}_{-0.3}$	6.7 ± 0.1	6.7 ± 0.1	6.8 ± 0.1
Diskline	inclination	degrees	65	65	65	65
Diskline	inner radius	GM c ⁻²	11	11	11	11
Diskline	normalization	ph cm ⁻² s ⁻¹	0.62 ± 0.16	0.47 ± 0.14	0.5 ± 0.2	0.45 ± 0.16
χ_r^2/dof			1.07/624	1.13/182	1.05/264	1.17/487

Note. Best-fit parameters of the spectral modeling described in Section 3.3. Uncertainties are quoted at 90% confidence. If no uncertainty is given, the parameter was held fixed. If no value is listed, then the component was not included in the model.

reflection spectra calculated for a hydrogen density of $n_{\text{H}} = 10^{18} \text{ cm}^{-3}$, using a grid in temperature (kT), ionization ($\log \xi$), and Fe abundance ($\log \text{Fe}$). As before, we kept the parameters for the absorption column and preburst components fixed. The temperature parameter of the reflection table was linked to the blackbody temperature, and the `rdblur` parameters were identical to those of the `diskline` component discussed above. This model yielded a reasonable description of the continuum (χ_r^2 of 1.2 for 628 dof), but left a large residual at 1 keV. Adding in a Gaussian component gave a good fit to the data at a χ_r^2 of 0.95 for 633 dof, with a normalization of $0.86 \pm 0.15 \text{ ph cm}^{-2} \text{ s}^{-1}$ and standard deviation of $0.09 \pm 0.02 \text{ keV}$. The best-fit parameters for the reflection component were $\log \xi = 3.79^{+0.11}_{-0.08}$, $\log \text{Fe} = 0.51^{+0.10}_{-0.24}$, and an unabsorbed bolometric reflection flux of $(1.87 \pm 0.13) \times 10^{-7} \text{ erg s}^{-1} \text{ cm}^{-2}$, indicating the reflection fraction is $F_{\text{refl}}/F_{\text{bb}} \approx 2.3$. Finally, we note that in this model, the photosphere blackbody had a temperature of $2.05 \pm 0.06 \text{ keV}$ and a radius of $6.6 \pm 0.7 \text{ km}$. While the temperature is consistent with the double blackbody model, the radius is significantly smaller.

The double blackbody and reflection models both provide a statistically acceptable description of the spectrum, and give a roughly equivalent interpretation. Since the double blackbody model is phenomenologically simpler, it can be fit robustly to much shorter integration times, yielding a higher time resolution view of the spectral evolution in the burst. In the following we will therefore focus our analysis on this model.

We extracted spectra from three other distinct time intervals during the burst: the pause (0.6 s), the dip (0.7 s), and the second peak (2 s). Each spectrum could be described with the double blackbody spectrum plus 6.7 keV `diskline` component. The second peak additionally required an emission line at 1 keV. These spectra are shown in Figure 2 and their best-fit parameters are listed in Table 1.

3.4. Time-resolved Spectroscopy

To investigate the full spectral evolution of the X-ray burst, we applied high-resolution time-resolved spectroscopy. We extracted 133 spectra from dynamically allocated intervals. Each interval was constructed to have at least 0.125 s of

exposure, and was increased as needed to include a minimum of 2000 counts. Each spectrum was then fit using the double blackbody model. Because the emission line components could not be reliably resolved over such short exposures, we did not include them in this analysis. The resulting evolution in spectral parameters is shown in Figure 3.

The time-resolved spectroscopy demonstrates that the hot ($\approx 2 \text{ keV}$) blackbody in our model can be understood as the emission from a neutron star photosphere that undergoes PRE between $t \approx 1 \text{ s}$ and $t \approx 13 \text{ s}$. The radius expansion is moderate, reaching a maximum radius of $\approx 15 \text{ km}$. The cool ($\approx 0.2 \text{ keV}$) blackbody, on the other hand, maintains a stable temperature through the burst, with its emitting area closely tracking the evolution of the overall flux. This trend further supports the idea that the soft excess tracks an interaction between the burst emission and the neutron star environment, such as the disk reflection model discussed in Section 3.3.

Considering the bolometric flux, we see that the burst emission reaches a stable peak of $(2.40 \pm 0.12) \times 10^{-7} \text{ erg s}^{-1} \text{ cm}^{-2}$ when the photosphere is at its largest extent. As the photosphere begins to contract, the flux begins to decrease. This cooling trend, however, is interrupted at $t \approx 15.5$. In the following $\approx 3 \text{ s}$, we see the bolometric flux holding constant, causing an excess over the cooling trend that coincides exactly with the second peak observed in the light curve. Hence, the spectroscopy confirms that the dip and second peak seen in the light curve are indeed astrophysical in origin rather than a passband effect.

Finally, we note a peculiar feature in the spectroscopic results: the temperature evolution of the photosphere shows two peaks, marking the start and end of the PRE phase. These start and end times coincide with the pause and the dip, respectively. Furthermore, both the pause and the dip have the same bolometric flux level of $(1.43 \pm 0.09) \times 10^{-7} \text{ erg s}^{-1} \text{ cm}^{-2}$.

3.5. Burst Oscillations

To search for burst oscillations, we constructed a 1/8192 s time resolution light curve in the 0.3–10 keV energy band. We then searched for coherent oscillations in a 10 Hz region centered on the known 401 Hz pulsar spin frequency by

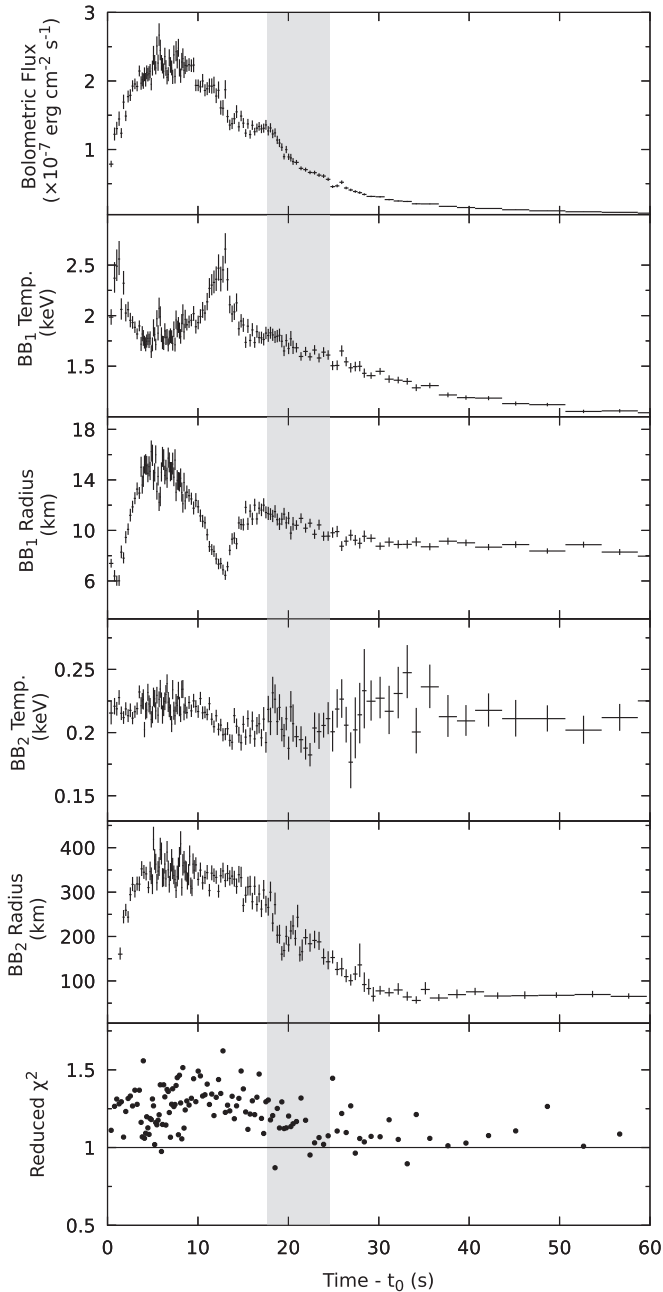


Figure 3. Time-resolved spectroscopy of the X-ray burst using a double blackbody model. The top panel shows the estimated bolometric flux, the middle four panels show the time evolution of the spectral parameters describing the burst emission (radii were calculated using a distance of 3.5 kpc), and the bottom panel gives the reduced χ^2 fit statistic. The gray band indicates the time interval where burst oscillations were detected. See the text for further details.

applying a sliding window search method (see, e.g., Bilous & Watts 2018, and references therein). Specifically, we used window sizes of $T = 1, 2,$ and 4 s, with strides of $T/10$ s. For each window position, we computed a power spectrum and searched for a signal power in excess of the expected noise distribution (van der Klis 1989). We detected a significant oscillation ($>3\sigma$) in all windows between $t = 17.7$ s and $t = 24.6$ s. The fractional sinusoidal amplitude¹⁴ of the burst

¹⁴ Sinusoidal amplitudes are a factor of $\sqrt{2}$ larger than fractional rms amplitudes.

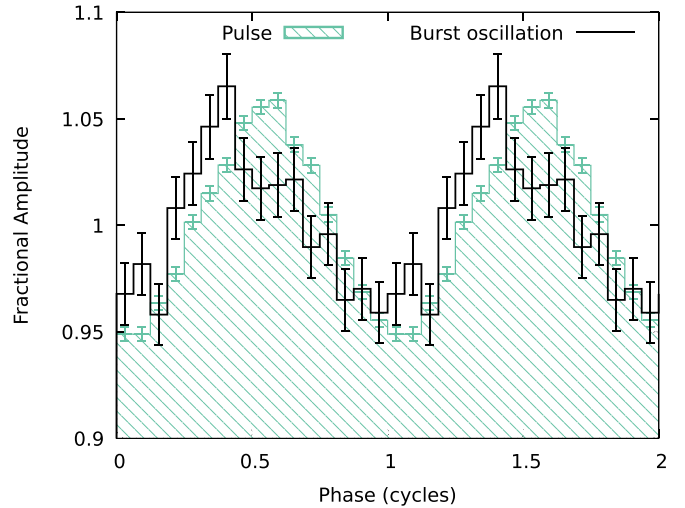


Figure 4. Waveform of the burst oscillation observed in SAX J1808, compared to the waveform of the accretion-powered pulsation as seen outside the X-ray burst interval.

oscillation was $(4.0 \pm 0.6)\%$, while the oscillation frequency was 401 Hz and did not show any significant drift.

Given the stability of the burst oscillation frequency, we folded the event times within the noted epoch on the pulsar spin period to obtain a waveform for the burst oscillation. For comparison, we also extracted the waveform of the persistent pulsations from the full ObsID, excluding the burst emission (see Bult et al. 2019 for a preliminary ephemeris). Both waveforms are shown in Figure 4. The burst oscillation has a similar profile and amplitude as the persistent pulsation, but appears to lead the pulse by $34^\circ \pm 7^\circ$.

To resolve the burst oscillation with respect to photon energy, we applied a sliding window to the instrument energy channel space, using a window size of 100 channels and strides of 10 channels. At each window position, we folded the selected data and measured the burst oscillation amplitude and phase. We then repeated this method for the nonburst data. The resulting amplitude spectra are shown in Figure 5. Although the averaged profiles are similar, the energy dependence of the burst oscillation is very different from that of the pulsar. Particularly notable is that the burst oscillation amplitude is mostly constant below ≈ 5 keV, but rises sharply at 6–7 keV.

4. Discussion

We detected a bright X-ray burst from SAX J1808 with *NICER*. The burst showed a peculiar light curve, with a notable pause during the rise and a double-peaked structure. Additionally, we detected significant burst oscillations in the cooling tail of the burst and emission features in the burst spectrum. We now discuss each of these findings.

4.1. Reflection

We find that the burst spectrum shows a strong excess at the lowest energies that requires the inclusion of a second blackbody in the spectral model. A similar strong soft excess was previously observed in SAX J1808 by in't Zand et al. (2013), who also report a marginal emission feature at 1 keV. In contrast to that work, we observed a significant emission feature at 1 keV, and a second feature at 6.7 keV. A similar

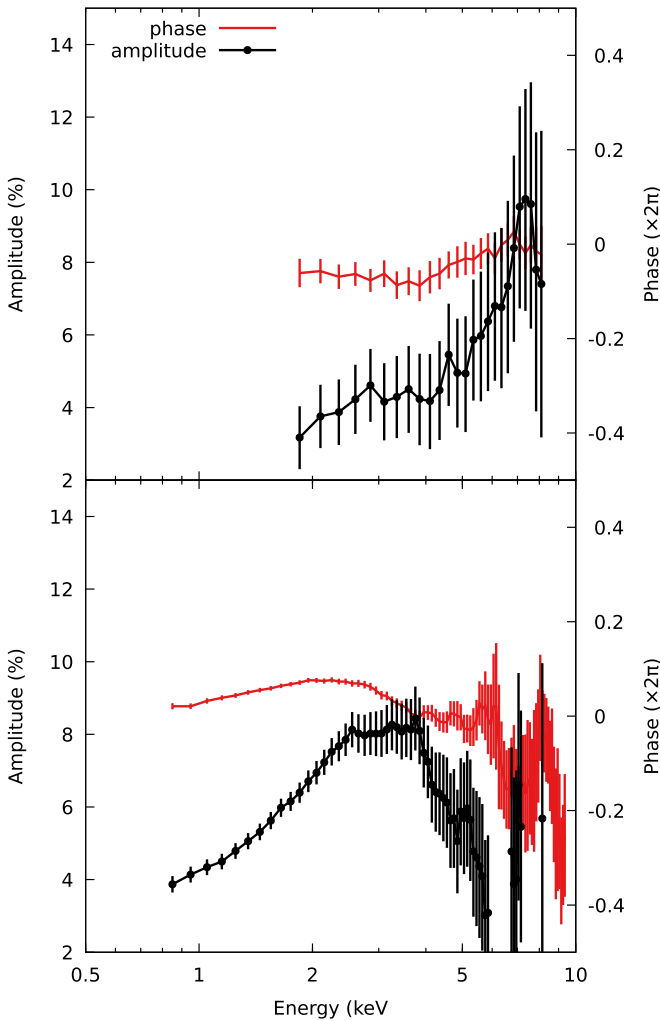


Figure 5. Top: energy dependence of the burst oscillation waveform. Bottom: same for the persistent pulsation observed outside the X-ray burst interval. Note that these data were computed using a sliding window, so adjacent points are correlated. Additionally, in order to look for decohering noise, we plot the waveform phase even if the amplitude is not formally significant.

complex of emission features has been seen in the intermediate-duration X-ray bursts from IGR J17062–6143 (Degenaar et al. 2013; Keek et al. 2017), which were associated with ionized Fe L and Fe K emission lines. Thus, the detection of these lines provides strong evidence that we are seeing the burst emission reflected from the accretion disk. Applying a physically motivated disk reflection model to our data (Section 3.3) indicates that such a reflection component provides a satisfactory description of the soft excess, but cannot fully account for the emission feature observed at 1 keV. We suggest that this may be due to the presence of additional elements not currently incorporated in these models (e.g., Ne). Additionally, this model fit indicated a strong reflection signal, which may indicate that the accretion disk structure is significantly impacted by the burst (He & Keek 2016; Fragile et al. 2018).

4.2. Spectral Evolution

The X-ray burst light curve shows a double-peaked structure. Given that the second peak in count rate occurs after the PRE

phase, and that this peak is reproduced (albeit less prominently) in the bolometric flux, we conclude that this feature is astrophysical in origin. A very similar double-peaked structure in an X-ray burst from 4U 1608–52 was recently observed with *NICER* (Jaisawal et al. 2019). Although that burst showed a hotter photosphere and lacked the strong soft excess that we detect in SAX J1808, the rebrightening phase is nearly identical in both bursts. In each case, the end of the PRE phase coincides with a pronounced dip in count rate, and is followed by a secondary peak.

Jaisawal et al. (2019) considered a number of plausible origins for the rebrightening of the burst flux, including the ignition of fresh material (Keek & Heger 2017), stalled thermonuclear flame spreading (Bhattacharyya & Strohmayer 2006), and waiting points in the rp-process (Fisker et al. 2004). Our observation of rebrightening in the X-ray burst from SAX J1808 does not rule out any of these proposed explanations. It does, however, add two new perspectives: first, in SAX J1808 the rebrightening coincides with the onset of burst oscillations, which may be difficult to reconcile with a flame spreading model. Second, in SAX J1808 the dip appears related to the pause during the rise. If this relation is real, then whatever physical mechanism underpins these features may also be related to the rebrightening.

4.3. Burst Oscillations

We found that the X-ray burst shows burst oscillations at the expected 401 Hz spin frequency. Comparing these oscillations with the accretion-powered pulsations, we find that the two waveforms are remarkably similar, but the burst oscillations lead the pulsations by $34^\circ \pm 7^\circ$. Similar results were reported from *RXTE* observations of burst oscillations in SAX J1808 observed during the cooling phase of an X-ray burst (Chakrabarty et al. 2003). The fact that the burst oscillations are so closely matched to the persistent pulsations in terms of their waveform, suggests that both must arise from geometrically similar, if not the same, confined emitting region (hot-spot) on the stellar surface. With this in mind, it is interesting to note that the *NICER* data indicate the waveform energy dependence of the burst oscillations is quite different from that of the persistent pulsations. Some of the differences may simply arise from the strong reflection component, which is likely not pulsed, and thus is expected to dilute the measured burst oscillation amplitude at low energies. A detailed spectral-timing analysis may be able to determine how much each of the spectral components is oscillating. Such an analysis, however, is beyond the scope of this initial work.

4.4. Eddington Limits

Finally, we note that our analysis of the light curve, the spectral evolution, and the timing behavior all indicate that each time interval where the *NICER* count rate of SAX J1808 is between 13,000 and 14,000 ct s^{-1} is somehow special. At these count rates, the burst rise pauses, the dip reaches its minimum, and burst oscillations appear. The bolometric flux measured at these times was $(1.43 \pm 0.09) \times 10^{-7} \text{ erg s}^{-1} \text{ cm}^{-2}$, which corresponds to a luminosity of $(2.08 \pm 0.13) \times 10^{38} \text{ erg s}^{-1}$. We note that this luminosity is consistent with the expected local Eddington limit of a hydrogen envelope of a neutron star (Lewin et al. 1993).

For spherically symmetric emission, the Eddington luminosity as measured by the observer is predicted as (Lewin et al. 1993; Suleimanov et al. 2017)

$$L_{\text{edd}} = \frac{4\pi GMc}{\kappa_{\text{T}}} \frac{1}{(1+z)}, \quad (1)$$

where M is the neutron star mass, G is the gravitational constant, c is the speed of light, and z is the gravitational redshift. Finally, $\kappa_{\text{T}} = 0.2(1+X)\text{cm}^2\text{g}^{-1}$ is the Thomson electron scattering opacity, with X being the hydrogen abundance in the atmospheric layer. Hence, we expect that the flux level at which PRE occurs differs depending on the material composition of the neutron star envelope. For a hydrogen layer with cosmic abundances ($X=0.73$), the predicted luminosity is $\approx 2.0 \times 10^{38}\text{erg s}^{-1}$, whereas the luminosity of a pure helium layer ($X=0$) is larger by a factor of 1.73. In SAX J1808, the ratio in bolometric flux between the peak and pause/dip is 1.68 ± 0.13 .

The following scenario now emerges for the X-ray burst evolution. As the critical ignition point is reached in the helium layer, the flame front quickly spreads across the stellar surface and an intense radiation field starts to diffuse outward. After about 0.5 s, the radiation pressure reaches the local Eddington limit of the hydrogen layer, causing that layer to expand. Meanwhile, the intensity of the radiation field continues to increase, either expelling or diluting the hydrogen layer, so that the observed spectrum becomes dominated by the PRE of the helium layer. Over the following 10 s, we observe the full helium PRE cycle, causing the photosphere to cool and then heat, as the envelope expands and then contracts. Once the envelope touches back down on the stellar surface, the burst flux is still comparable to hydrogen Eddington limit, although at the time this touchdown occurs, there will likely have been some mixing of the atmospheric layers. Subsequently, the photosphere cools, while the radius grows, and then, after about 4–5 s, the rebrightening mechanism activates and quickly thereafter the burst oscillations appear. The photosphere continues to cool, and after about 10 s both the rebrightening and oscillations switch off.








The flux levels of the pause and peak are highly suggestive that we are seeing both the hydrogen and helium Eddington limits in a single X-ray burst. The evolution of the hardness ratio around the pause further supports the interpretation that this stall in the rise is related to the expanding hydrogen layer. The link between the pause and the dip is weaker, but highly suggestive, and may yet provide the insight required to uncover the physics behind intrinsic rebrightening during the tail of an X-ray burst.

This work was supported by NASA through the *NICER* mission and the Astrophysics Explorers Program, and made use of data and software provided by the High Energy Astrophysics Science Archive Research Center (HEASARC). P.B. was supported by an NPP fellowship at NASA Goddard Space Flight Center. G.K.J. was supported by the Marie Skłodowska-Curie Actions grant No. 713683 (H2020). D.A. acknowledges support from the Royal Society. R.M.L. acknowledges the support of NASA through Hubble Fellowship Program grant *HST-HF2-51440.001*.

Facilities: ADS, HEASARC, *NICER*.

Software: heasoft (v6.26), nicerdas (v6a), xspec (v12.10).

ORCID iDs

Gaurava K. Jaisawal  <https://orcid.org/0000-0002-6789-2723>
 Tolga Güver  <https://orcid.org/0000-0002-3531-9842>
 Tod E. Strohmayer  <https://orcid.org/0000-0001-7681-5845>
 David R. Ballantyne  <https://orcid.org/0000-0001-8128-6976>
 Deepto Chakrabarty  <https://orcid.org/0000-0001-8804-8946>
 Jérôme Chenevez  <https://orcid.org/0000-0002-4397-8370>
 Sebastien Guillot  <https://orcid.org/0000-0002-6449-106X>
 Renee M. Ludlam  <https://orcid.org/0000-0002-8961-939X>

References

- Arnaud, K. A. 1996, in ASP Conf. Ser. 101, *Astronomical Data Analysis Software and Systems V*, ed. G. H. Jacoby & J. Barnes (San Francisco, CA: ASP), 17
- Ballantyne, D. R. 2004, *MNRAS*, 351, 57
- Ballantyne, D. R., & Everett, J. E. 2005, *ApJ*, 626, 364
- Bhattacharyya, S., & Strohmayer, T. E. 2006, *ApJL*, 636, L121
- Bildsten, L., & Chakrabarty, D. 2001, *ApJ*, 557, 292
- Bilous, A. V., & Watts, A. L. 2018, arXiv:1812.10684
- Bult, P., & van der Klis, M. 2015, *ApJ*, 806, 90
- Bult, P. M., Gendreau, K. C., Arzoumanian, Z., et al. 2019, *ATel*, 13001, 1
- Cackett, E. M., Altamirano, D., Patruno, A., et al. 2009, *ApJL*, 694, L21
- Chakrabarty, D., & Morgan, E. H. 1998, *Natur*, 394, 346
- Chakrabarty, D., Morgan, E. H., Muno, M. P., et al. 2003, *Natur*, 424, 42
- Degenaar, N., Ballantyne, D. R., Belloni, T., et al. 2018, *SSRv*, 214, 15
- Degenaar, N., Miller, J. M., Wijnands, R., Altamirano, D., & Fabian, A. C. 2013, *ApJL*, 767, L37
- Di Salvo, T., Sanna, A., Burderi, L., et al. 2019, *MNRAS*, 483, 767
- Fabian, A. C., Rees, M. J., Stella, L., & White, N. E. 1989, *MNRAS*, 238, 729
- Fisker, J. L., Thielemann, F.-K., & Wiescher, M. 2004, *ApJL*, 608, L61
- Fragile, P. C., Ballantyne, D. R., Maccarone, T. J., & Witry, J. W. L. 2018, *ApJL*, 867, L28
- Galloway, D. K., & Cumming, A. 2006, *ApJ*, 652, 559
- Galloway, D. K., Goodwin, A. J., & Keek, L. 2017, *PASA*, 34, e019
- Galloway, D. K., Muno, M. P., Hartman, J. M., Psaltis, D., & Chakrabarty, D. 2008, *ApJS*, 179, 360
- Gendreau, K., & Arzoumanian, Z. 2017, *NatAs*, 1, 895
- Goodwin, A. J., Galloway, D. K., Heger, A., Cumming, A., & Johnston, Z. 2019a, *MNRAS*, in press (doi:10.1093/mnras/stz2638)
- Goodwin, A. J., Russell, D. M., Galloway, D. K., et al. 2019b, *ATel*, 12993
- Grindlay, J. E., Marshall, H. L., Hertz, P., et al. 1980, *ApJL*, 240, L121
- Hartman, J. M., Patruno, A., Chakrabarty, D., et al. 2008, *ApJ*, 675, 1468
- He, C. C., & Keek, L. 2016, *ApJ*, 819, 47
- in't Zand, J. J. M., Cornelisse, R., Kuulkers, E., et al. 2001, *A&A*, 372, 916
- in't Zand, J. J. M., Galloway, D. K., Marshall, H. L., et al. 2013, *A&A*, 553, A83
- in't Zand, J. J. M., Heise, J., Muller, J. M., et al. 1998, *A&A*, 331, L25
- Jahoda, K., Markwardt, C. B., Radeva, Y., et al. 2006, *ApJS*, 163, 401
- Jaisawal, G. K., Chenevez, J., Bult, P., et al. 2019, *ApJ*, 883, 61
- Keek, L., Arzoumanian, Z., Bult, P., et al. 2018a, *ApJL*, 855, L4
- Keek, L., Arzoumanian, Z., Chakrabarty, D., et al. 2018b, *ApJL*, 856, L37
- Keek, L., & Heger, A. 2017, *ApJ*, 842, 113
- Keek, L., Iwakiri, W., Serino, M., et al. 2017, *ApJ*, 836, 111
- Lewin, W. H. G., van Paradijs, J., & Taam, R. E. 1993, *SSRv*, 62, 223
- Makishima, K., Maejima, Y., Mitsuda, K., et al. 1986, *ApJ*, 308, 635
- Narayan, R., & Heyl, J. S. 2003, *ApJ*, 599, 419
- Papitto, A., Di Salvo, T., D'Ai, A., et al. 2009, *A&A*, 493, L39
- Parikh, A. S., & Wijnands, R. 2019, *ATel*, 13000
- Patruno, A., Jaodand, A., Kuiper, L., et al. 2017, *ApJ*, 841, 98
- Russell, D. M., Goodwin, A. J., Galloway, D. K., et al. 2019, *ATel*, 12964
- Sanna, A., Di Salvo, T., Burderi, L., et al. 2017, *MNRAS*, 471, 463
- Standish, E. M. 1998, *JPL Planetary and Lunar Ephemerides, DE405/LE405*, JPL Interoffice Memo 312.F-98-048 (Pasadena, CA: NASA Jet Propulsion Laboratory)
- Strohmayer, T. E., Altamirano, D., Arzoumanian, Z., et al. 2019, *ApJL*, 878, L27
- Suleimanov, V. F., Poutanen, J., Näätäjä, J., et al. 2017, *MNRAS*, 466, 906
- van der Klis, M. 1989, in *Timing Neutron Stars*, ed. H. Ögelman & E. P. J. van den Heuvel (Dordrecht: Kluwer), 27

Verner, D. A., Ferland, G. J., Korista, K. T., & Yakovlev, D. G. 1996, *ApJ*, 465, 487
Weinberg, N. N., Bildsten, L., & Schatz, H. 2006, *ApJ*, 639, 1018
Wijnands, R., & van der Klis, M. 1998, *Natur*, 394, 344
Wilms, J., Allen, A., & McCray, R. 2000, *ApJ*, 542, 914

Worpel, H., Galloway, D. K., & Price, D. J. 2013, *ApJ*, 772, 94
Yu, H., & Weinberg, N. N. 2018, *ApJ*, 863, 53
Zdziarski, A. A., Johnson, W. N., & Magdziarz, P. 1996, *MNRAS*, 283, 193
Życki, P. T., Done, C., & Smith, D. A. 1999, *MNRAS*, 309, 561